Korean J. Chem. Eng., 39(5), 1165-1181 (2022)
DOI: 10.1007/s11814-021-1035-6

pISSN: 0256-1115
eISSN: 1975-7220

Dynamic behavior of an ellipsoidal bubble contaminated by surfactant near a vertical wall

Enbo Ju*,, Runze Cai*,**, Haopeng Sun*,**, Ying Fan*,**, Wenyi Chen*,**,†, and Jiao Sun*,**,***,†**

*Department of Process Equipment and Control Engineering, Hebei University of Technology, Tianjin 300130, China
**National-Local Joint Engineering Laboratory for Energy Conservation in Chemical Process Integration and Resources Utilization, School of Chemical Engineering, Hebei University of Technology, Tianjin 300130, China
***Department of Mechanics, School of Mechanical Engineering, Tianjin University, Tianjin 300350, China
(*Received 6 September 2021 • Revised 28 November 2021 • Accepted 2 December 2021*)

Abstract−Adding a small amount of surfactant to gas-liquid two-phase flow can markedly change bubble behavior, which has crucial application value in nuclear energy, petrochemical, chemical, and environmental engineering. In this paper, the dynamic behavior of a single ellipsoidal bubble (Re~800) contaminated by surfactant rising near a vertical wall in stagnant liquid is studied using the shadow method. The effects of different concentrations of sodium dodecyl sulfate solution (100 ppm, 400 ppm, 800 ppm) and initial dimensionless distances on bubble dynamics were compared. The dynamic parameters, shape oscillation, force, and energy of the bubble were analyzed. The results show that the critical initial dimensionless distance at which the collision occurs is decreased due to a dimensionless distance change from 3.3 to 0.23, accelerating the transition from zigzag to spiral movement. Transverse movement of the contaminated bubble is restrained. Because of the Marangoni effect caused by the surfactant, the boundary condition changes from zero shear to non-zero shear, resulting in a decrease in velocity and an increase in the drag coefficient. As the surfactant concentration increases, the lift coefficient does not significantly change with concentration variations. The influences of the wall effect on velocity and drag gradually weaken. Comparing free-rising and collision conditions, the aspect ratio of the contaminated bubble is distinct from the regularity of a clean bubble. The surfactant also changes the wall-normal velocity frequency and symmetrical shape frequency and inhibits energy conversion during collision.

Keywords: Bubble Dynamics, Gas-liquid Two-phase, Wall Effect, Marangoni Effect, Bubble-wall Collision

INTRODUCTION

The rising behavior of bubbles in liquid due to gravity was initially studied many centuries ago and is still a very interesting problem with considerable significance in the process of heat and mass transfer [1]. Bubbles can be contaminated by surfactants and dynamic characteristics change significantly, leading to essential changes in heat and mass transfer at the gas-liquid interface [2]. For example, in the flotation process, the addition of surfactants can stabilize the gas-liquid interface to reduce the bubble polymerization rate and enhance the interaction between the phases. Surfactants also play a crucial role in the safety and efficiency of nuclear reactors and bubble-cap columns. In these environments, baffles or walls are usually set to control the residence time, movement, and distribution regularity of bubbles in the dispersion phase [3]. Therefore, the dynamic characteristics of bubbles contaminated by surfactants need to be studied to contend with the design requirements of chemical and energy industries.

Surfactant molecules are composed of a hydrophilic head and a hydrophobic tail, tending to aggregate at the gas-liquid interface and form a single molecular layer [4]. It interacts with the fluid molecule, which reduces the surface tension and changes the mechanical properties of the interface [5].

Marangoni stress is induced due to the non-uniform distribution of surface tension. The surfactant molecules are gathered at the rear of the bubble to the front surface, thus reducing the fluidity of the interface [6,7]. The Marangoni stress changes the interfacial properties, which finally affects the dynamic characteristics of a bubble [8]. As it is difficult to control the contaminated degree of the bubble interface in experiments, the behavior of bubble movement is usually changed by adjusting the surfactant concentration, which corresponds to the surface tension coefficient (σ) and dimensionless number such as Reynolds number ($Re=\rho_l U d_{eq} \mu^{-1}$), Eötvös number ($Eo=g d_{eq}^2(\rho_l-\rho_g)\sigma^{-1}$), Weber number ($We=\rho_l U^2 d_{eq}\sigma^{-1}$), and Morton number ($Mo=(\rho_l-\rho_g)g\mu_l^4\sigma^{-3}\rho_l^{-2}$), where d_{eq}, ρ, and μ are equivalent diameter of bubble, density and dynamic viscosity, respectively.

The surfactant has an important influence on the movement [9]. The three-dimensional motion of the bubble is changed drastically with various surfactant concentrations. Types of bubble motions have been strongly dependent on Reynolds number in the case of a free-slip and a no-slip condition [10]. Rodrigue et al. [11] studied that the presence of surfactants is influenced the bubble velocity at various concentrations of sodium dodecyl sulfate (SDS) 0-500 ppm, but also leads to an empirical correlation to calculate the equivalent diameter. The surfactant reduces the terminal velocity of bubbles, especially in the nearly spherical regime where the bubble behaves similarly to a solid sphere. The terminal velocity of bub-

†To whom correspondence should be addressed.
E-mail: cwy63@126.com, sunjiao@hebut.edu.cn

bles approaches that of an equivalent solid sphere [12]. Coenot et al. [13] found that a surfactant has a great influence on the flow around spherical bubbles, slowing the flow behind the bubbles, resulting in the sharp increase of drag coefficient. Fei et al. [14] found that the vortex structure gradually is strengthened as the contaminated degree of spherical bubbles increases, which proves that the contaminated bubble has a greater drag force.

The surfactant can effectively control the shape of bubbles and inhibit deformation. At a certain concentration range, the bubble size will decrease as the concentration increases [15]. Tzounakos et al. [16] studied that the effect of SDS concentration on the terminal velocity and shape of a rising bubble. SDS with a concentration below 30 ppm has no obvious effect on bubble shape. The decrease of bubble velocity is mainly due to the decrease of interface fluidity rather than the change of bubble shape. Aoyama et al. [17] studied different concentrations (maximum concentration to critical micelle concentration) and different kinds of surfactants (Triton X-100, SDS, 1-OCtanol, and 1-decanol.). They found a relationship between the aspect ratio of bubble and dimensionless number (Re, Eo) and surface tension coefficient (σ).

On the other hand, bubbles will be affected by the wall to change the motion behavior [18]. Due to the wall effect at different dimensionless wall distances S^*, bubbles may experience repeated bounds, slide along the wall, or rise spirally [19]. The dimensionless distance S^* is defined as $S^*=S/r_{eq}$, where S is the initial distance between the nozzle and the wall, r_{eq} is the equivalent radius of the bubble. As S^* increases, bubble-wall collision frequencies and the corresponding repulsive lift from a wall will decrease. When the Reynolds number Re<40, the bubble is far away from the wall. Because the vorticity generated by the shear-free condition on the rising bubble surface diffuses in the wake and interacts with the wall to cause repulsive lift [20]. When Re<100, different motions of rising spherical bubbles are observed under the action of repulsive force and wall-normal force [21]. When the gap between the bubble and the wall becomes narrower due to this attraction, the influence of viscosity in the thin liquid layer causes the lift to reverse and the rising bubble bounces off the wall [22]. When 1≤Re≤300, the existence of the wall could lead to the increase of drag, the magnitude and direction of the lift acting on bubbles depending on Re and the distance between bubble and wall [23].

Deformation is related to the energy conversion when the bubbles collide with the wall. Zaruba et al. [24] predicted the change of bubble bouncing motion with liquid velocity. When the liquid velocity is low, bubbles gain extra energy from shape oscillation to compensate for the damping effect caused by colliding with the wall, so that the bouncing amplitude remains almost constant. Jeong et al. [25] found that surface deformation is closely related to energy transmission during the rising process of bubbles. When the bubbles collide with the wall, the surface energy compensates for the lack of kinetic energy to make the deformable bubble keep relatively constant motion. Chen et al. [26] studied the energy conversion and the shape oscillation of deformable bubbles near the wall. The frequency of the two modes is calculated through the major axis and minor axis of the bubble in space. The characteristic frequency is measured by the frequency spectrum.

Although extensive research has been performed, such research is generally restricted to free-rising spherical bubbles contaminated by surfactants and clean bubbles rising near walls along a zigzag trajectory. To the best of our knowledge, research on the dynamics of ellipsoidal bubbles contaminated by surfactants rising near walls along a spiral trajectory is limited, thus failing to meet actual industrial requirements. In a nuclear reactor, sewage treatment, and bubble-cap column, the presence of wall and surfactant exerts shear stress on the bubble, respectively. Which factors dominate the dynamic behavior of bubbles is unknown. This is of great significance to the chemical and energy design industry. We believe that the behavior of a bubble is closely related to the surfactant concentration. Under the influence of surfactant and wall, the dominant factors of behavior at various concentrations are different.

We conducted experiments on the dynamic behavior of an ellipsoidal bubble (Re~800) contaminated by surfactant rising near a vertical wall in stagnant water. Sodium dodecyl sulfate (SDS) was used as the experimental surfactant. SDS is the most common surfactant present in soaps and detergents and is the most frequently occurring surfactant in wastewaters. We systematically changed the surfactant concentration SDS and the initial distance between the bubble and the wall. The trajectory, velocity, force, deformation, and energy change of contamination bubbles near a wall were analyzed to provide reference data for the study of nuclear energy and chemical engineering, such as nuclear reactors and bubble-cap columns.

EXPERIMENTS

1. Experimental Setup

As shown in Fig. 1(a), the experimental device uses the shadow method to record bubbles, which is similar to the previous study of Jeong [25]. The tank is an acrylic cube container (x=300 mm, y=650 mm, z=300 mm) with a stainless steel nozzle (outer diameter 1.48 mm, inner diameter 1.12 mm) located at the center of the bottom. The acrylic plate (x=20 mm, y=580 mm, z=200 mm) is a wall constraint that can be moved along the x-axis through the screw slider mechanism. After moving the wall, the liquid in the tank is let stand for 10 minutes to ensure it is quiescent. As shown in Fig. 1(b), S is the initial distance between the nozzle and the wall. The single bubble jets vertically from the nozzle. A bubble generated from the air pump through the nozzle rises due to buoyancy in quiescent liquid. The bubble frequency is adjusted by adopting a micro gas flow regulating valve including a pressure regulator and solenoid valve. The interval between two bubbles is about 15 s to avoid the interference of the previous bubble wake on the next bubble trajectory [27]. The shadow light source is composed of two LED lamps (50 W) and diffusion plates. The acquisition frequency of the CCD camera (Image MX, La Vision, Germany, resolution 2,048×2,048) is 180 Hz and the recording area is 50 mm×140 mm. The camera is used for synchronously studying the shooting behavior of a rising bubble from two orthogonal azimuth angles. Each condition was measured 30 times to ensure the repeatability of experimental motion type. The recording area is arranged 19 cm above the nozzle outlet to avoid capturing the transition from zigzag to spiral track caused by vortex accumulated on the bubble surface [28].

To change the range of experimental conditions, the liquid properties and wall distance are changed. Liquid density (ρ), dynamic

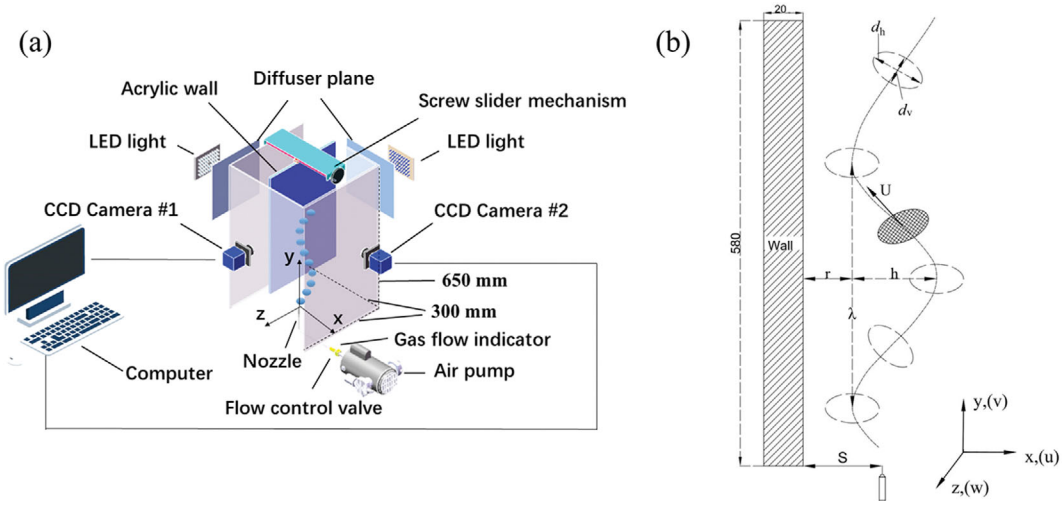

Fig. 1. (a) Experimental set-up for a single bubble rising near a vertical wall in a stagnant liquid tank, (b) Modelling of a periodically bouncing trajectory and definitions of bubble geometry.

Table 1. Properties of the liquids in the experiment

Liquid	C (ppm)	ρ_l (kg/m^3)	σ (mN/m)	μ (mPa·s)	Mo
Pure water	0	998	72.85	1.1	3.71×10^{-11}
Fluid 1	100	999	65.67	1.15	6.05×10^{-11}
Fluid 2	400	1,013	51.49	1.16	1.28×10^{-10}
Fluid 3	800	1,016	42.24	1.2	2.65×10^{-10}

viscosity (μ), and surface tension coefficient (σ) are measured by DH-300 DahoMeter, NDJ-79 PX, and DAS30 KRUSS, respectively. Table 1 list the properties of several SDS solutions used in this study, among which Morton number ($Mo=(\rho_l-\rho_g)g\mu_l^4\sigma^{-3}\rho_l^{-2}$) shows the liquid properties, C is the surfactant concentration. The experimental temperature is kept at room temperature 20±1 °C and the air density ρ_g=1.22 kg/m^3. The experimental concentration is lower than the critical micelle concentration (CMC).

2. Image Processing Techniques and Measurement Uncertainties

As shown in Fig. 2, the digital image processing algorithm includes four steps to detect bubbles from digital images: image preprocessing, image threshold segmentation, image filling, and bubble parameter extraction [29]. Image preprocessing includes gray scale conversion and image filtering. First, we set the optimal gray threshold to distinguish bubbles from background to binarize the original image. Then we applied a Sobel filter to evaluate the gray gradient of each pixel to detect the edge of bubbles. Based on detecting the bubble contour, some points with uniform spacing were selected on the edge of the bubble. Each point on the edge is connected to a point inside the bubble (the guessed center of the bubble). The bubble can be divided into several parts, and the actual bubble center is determined by calculating the center of gravity of each part.

Eqs. (1)-(2) are used to calculate the instantaneous velocity and the equivalent diameter of bubble.

$$U=\frac{\sqrt{(x_i-x_{i-1})^2+(y_i-y_{i-1})^2+(z_i-z_{i-1})^2}}{\Delta t} \quad (1)$$

$$d_{eq}=\sqrt[3]{d_h^2 d_v} \quad (2)$$

where x_i, y_i, z_i are the bubble centroid coordinates, x_{i-1}, y_{i-1}, z_{i-1} are the bubble centroid coordinates in the previous frame. d_h and d_v are the horizontal axis and the vertical axis, respectively.

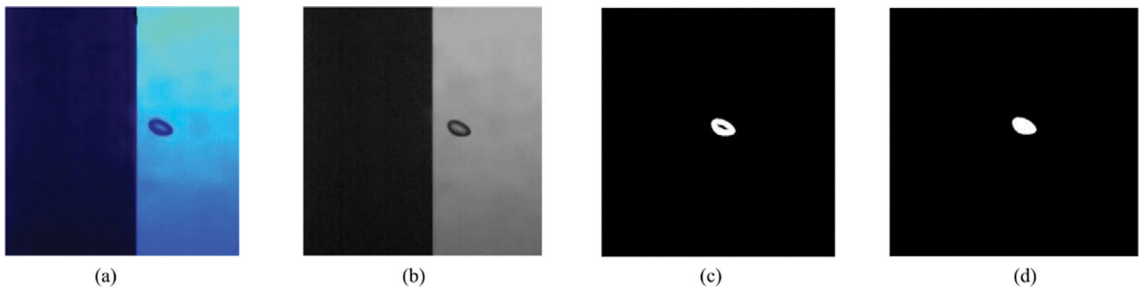

Fig. 2. Image processing procedure.

In this experiment, the equivalent diameter of the bubble is 3.24 mm under the pure water condition. As the surfactant concentration increases, the equivalent diameter of bubbles gradually decreases. The equivalent diameter of bubble d_{eq} ranges from 3.24 mm to 2.9 mm. The range of Reynolds number is 470-800. The range of Eötvös number is 1.41-1.98. The range of Weber number is 2.02-3.01.

The uncertainty of this experiment mainly includes the measurement of bubble diameter and centroid position. The diameter uncertainty is determined by digital image processing [30]. When the bubble does not collide with the wall, the maximum error of the bubble edge recognition is ±1 pixel. The maximum uncertainty of bubble diameter is less than 3%. When the bubble collides with the wall, the maximum error of bubble edge recognition is ±2 pixel. The uncertainty of bubble diameter is less than 5%. The uncertainty of centroid position is mainly due to the limited number of points used in the average calculation. In this paper, the time interval between two consecutive frames is 12 ms, the uncertainty of centroid position can also be ignored.

RESULTS AND DISCUSSION

1. Near-wall Rising behavior of a Contaminated Bubble

Figs. 3 and 4 show the trajectories of the rising bubble in the x-

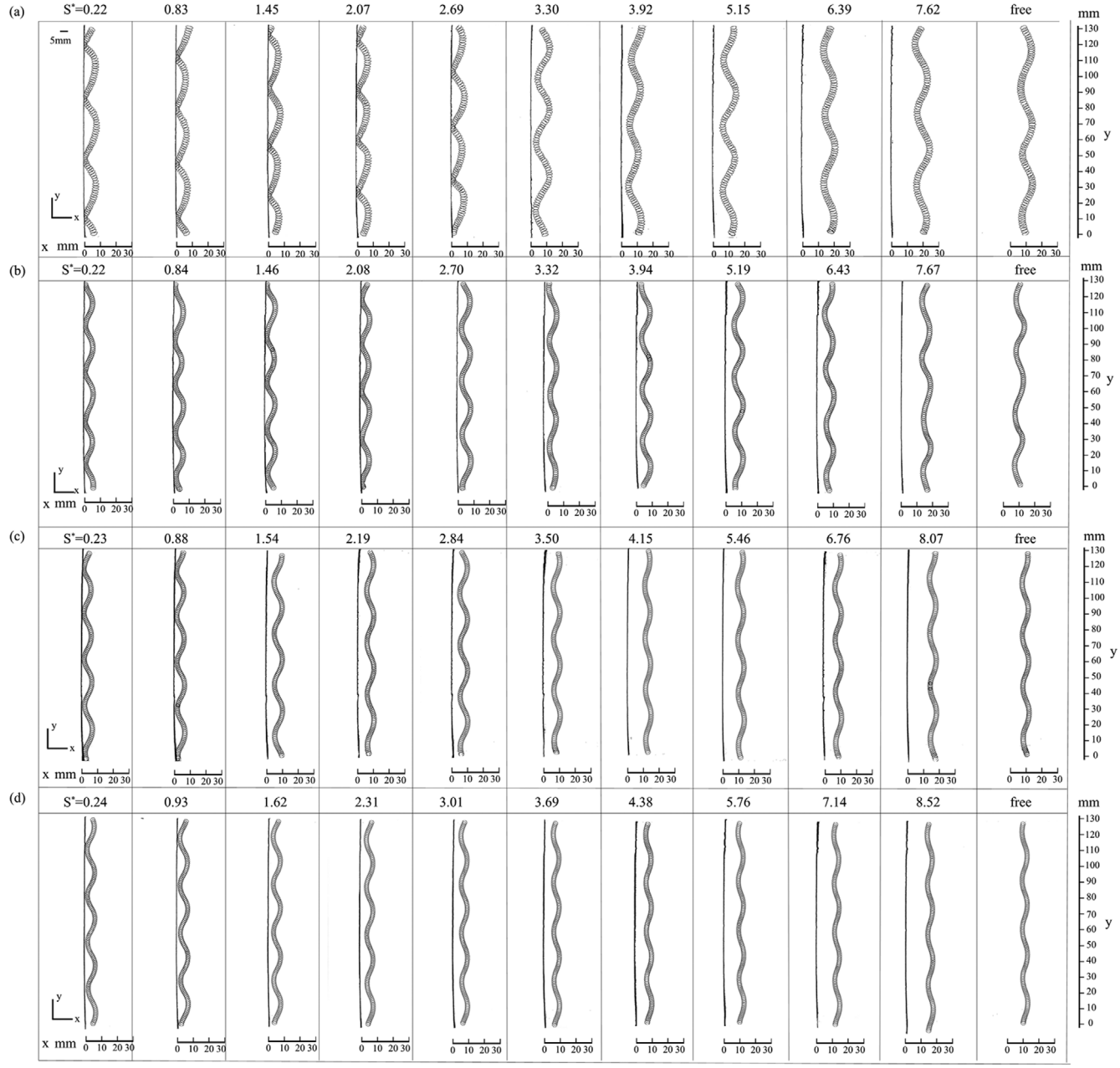

Fig. 3. Effect of different surfactant concentrations on the trajectories of rising bubbles in the x-y plane: (a) pure water, (b) 100 ppm, (c) 400 ppm, and (d) 800 ppm.

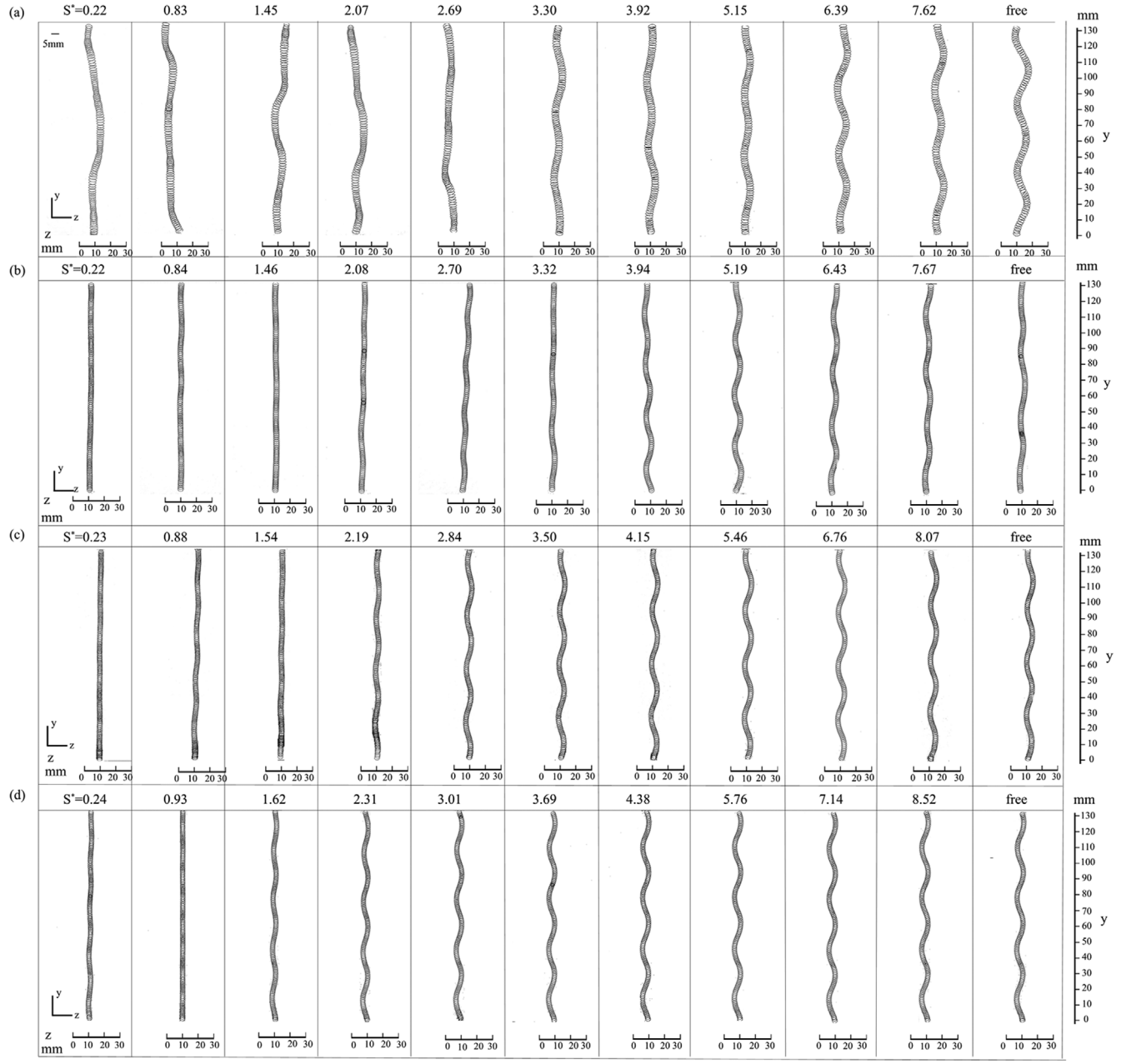

Fig. 4. Effect of different surfactant concentrations on the trajectories of rising bubbles in the y-z plane: (a) pure water, (b) 100 ppm, (c) 400 ppm, and (d) 800 ppm.

y plane and y-z plane at different initial dimensionless distances and concentrations. The trajectory of the bubble without constraint is a two-dimensional zigzag trajectory in the x-y, y-z planes and a three-dimensional spiral trajectory in space. When $S^*<3.3$, the rising trajectory of the bubble is significantly affected by the wall effect in pure water. Periodic collision occurs between the bubble and the wall. The trajectory of the x-y plane is a two-dimensional zigzag, and the trajectory of the y-z plane tends to be straight or chaotic. When $S^*>3.3$, the wall effect is weakened, and the bubble trajectory changes from slight oscillation to large oscillation in the y-z plane. Finally, it evolves into a three-dimensional spiral trajectory in space. After surfactant addition, the bubble is contaminated by the surfactant. When the bubble collides with the wall periodically, the chaotic trajectory of the y-z plane disappears and becomes straight. When the bubbles collide with the wall, the critical initial dimensionless distance at which the collision occurs S^* is 2.08 at 100 ppm. At 400 ppm and 800 ppm, the critical initial dimensionless distance at which the collision occurs S^* is 0.88 and 0.24, respectively. Surfactant reduces the critical initial dimensionless distance at which the collision occurs S^*. On the other hand, as the surfactant concentration increases, the change of initial dimensionless distance S^* shows the trajectory more quickly changes from a straight to a zigzag trajectory in the y-z plane. Surfactant accelerates the transition from a zigzag to a spiral trajectory in three di-

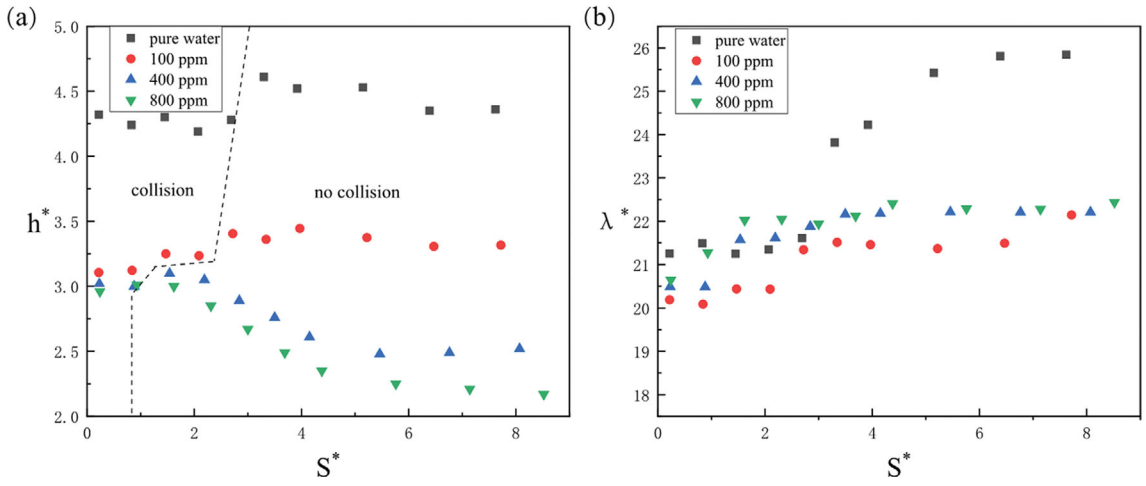

Fig. 5. Effects of dimensionless amplitude h^* and dimensionless wavelength λ^* as a function of dimensionless initial wall distance S^* at various surfactant concentrations; (a) dimensionless amplitude h^* (b) dimensionless wavelength λ^*.

mensions.

Trajectory instability of rising bubbles is a direct manifestation of wake instability [31]. Bubbles rise with a three-dimensional spiral trajectory in free space, and the bubble wake is a double spiral [27]. When a bubble rebounds on a wall, a symmetrical vortex tube structure is formed due to the wall limitation, which causes the bubble to rebound repeatedly in a zigzag motion [32]. The wake structure is weakened by the wall effect with the initial distance, and the trajectory of the bubble transitions to a three-dimensional spiral trajectory. Due to the influences of the velocity boundary layer and wake structure, the surfactant has a considerable influence on the flow around bubbles. As the surfactant concentration increases, the vortex structure becomes stronger, which will delay the rising movement of the bubble [13,14]. Due to the Marangoni effect, the wake of bubble contamination is wider and shorter than that in pure water [33]. As the thickness of the velocity boundary layer increases, the bubble cannot rapidly discharge the surrounding liquid during collision. As a result, the change in the vortex structure reduces the critical value of path instability.

Surfactant produces Marangoni stress on the surface of the bubble, which has a strong inhibitory effect on the transverse movement of the bubble [10]. Some researchers had proposed path fitting Eqs. (3)-(5) from a medium Re to a high Re in pure water [21,25, 26,34]. Due to the change in the surfactant concentration, these models cannot sufficiently fit the current experimental data.

$$y=\frac{h}{2}\left[1+\sin\left(\frac{2\pi}{\lambda}\right)l\right]+r \tag{3}$$

$$\lambda=\frac{1}{n}\sum_{1}^{n}\lambda_i \tag{4}$$

$$h=\frac{1}{n}\sum_{1}^{n}h_i \tag{5}$$

Here, h, λ, l and r are the amplitude, wavelength, height, and horizontal displacement of the periodic trajectory, respectively. The amplitude and wavelength of the trajectory are calculated by averaging the distances between two adjacent peaks along the trajectory in a set of data. Figs. 5(a) and 5(b) show the dimensionless amplitude ($h^*=h/r_{eq}$) and dimensionless wavelength of trajectory ($\lambda^*=\lambda/r_{eq}$) plotted as a function of dimensionless distance, respectively. We find that the amplitude and wavelength of contaminated bubble trajectories decreased compared with those under pure water conditions.

When clean bubbles collide with a wall, the amplitude of trajectory changes in a small range. When bubbles do not collide with the wall ($S^*>3.30$), the amplitude of trajectory increases rapidly and reaches the maximum value. With increasing S^*, bubbles gradually transition from two-dimensional zigzag motion to three-dimensional spiral motion, and the amplitude decreases. At 100 ppm, bubbles are contaminated by surfactant, and the amplitude decreases by approximately 24%, but the overall change is similar to that in pure water. Different from the case with a low concentration, when the concentration reaches 400 ppm, the amplitude gradually decreases to less than that in the case of collision with the wall. Surfactant inhibits the surface activity of a bubble and its internal flow circulation. As the concentration increases, the dynamic behavior of the bubble develops into a solid sphere. When the concentration is 800 ppm, the amplitude continues to decrease, but the decreasing trend slows. The effect of wall constraint on amplitude of trajectory is weakened with increasing concentration.

The wavelength of trajectory is almost unchanged when the bubble collides with a wall in pure water. The wavelength of trajectory increases instantaneously without collision. After surfactant addition, the wavelength changes. At 100 ppm, the wavelength is markedly decreased. As the concentration increases, with a similar wall position S^*, the wavelength shows an upward trend. Compared with that at 400 ppm and 800 ppm concentrations, the wavelength remains from 20.5 to 22.5. The wavelength is mainly affected by collision factors and is less affected by changes in concentration and wall distance.

2. Mean and Instantaneous Velocity of Rising Bubble

Fig. 6(a) shows the relationship between the mean velocity of bubbles and the dimensionless wall distance. As the wall distance

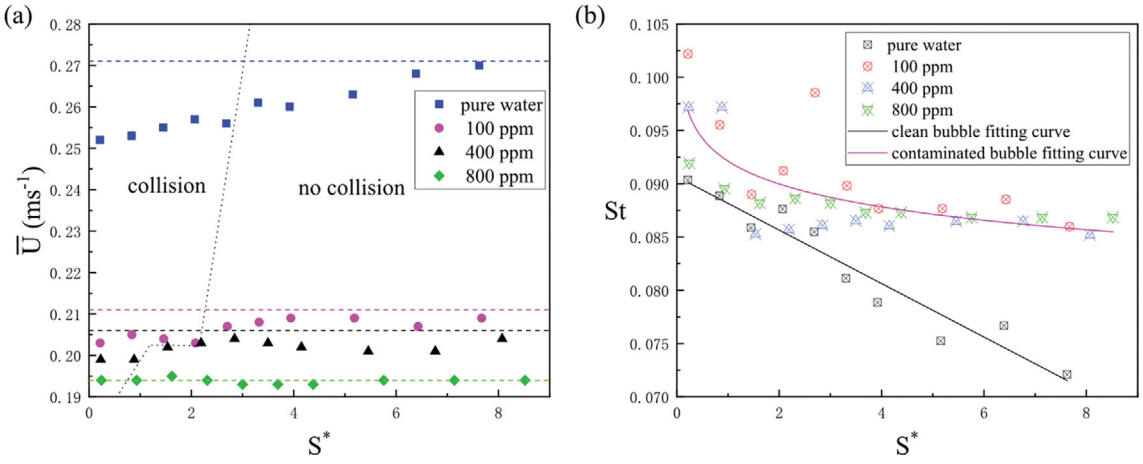

Fig. 6. Effects of the mean velocity of a rising bubble $\overline{U}$ and Strouhal number St as a function of dimensionless initial wall distance S^* at various surfactant concentrations: (a) the mean velocity of a rising bubble $\overline{U}$; dotted line: the free-rising case of the bubble (b) Strouhal number St.

increases, the mean velocity of a clean bubble gradually increases. When the dimensionless distance reaches approximately 8, the velocity approaches that of a free-rising bubble. The vortex shedding caused by collision increases the shearing effect of the fluid around the bubble, thus diminishing the bubble velocity [32]. After surfactant is added, the mean velocity of the bubble decreases obviously. For pure water conditions, the velocity at the time of collision is lower than the velocity without collision. When the concentration is 100 ppm, the velocity change trend of the contaminated bubble is the same as that of the clean bubble. At 400 ppm, the range of change is further reduced. However, when the concentration is 800 ppm, the mean velocity of the bubble is almost unchanged. The influence of the wall effect on the mean velocity of the bubble decreases with the concentration, and the Marangoni effect gradually dominates. Because of the hardening effect of the surfactant and suppression of the internal circulation on the contaminated bubble, the rigidity effect of the bubble increases. The surfactant causes the vortex to become shorter and stronger, which leads to a weaker wall shear effect and causes the mean velocity to decrease.

Path oscillation of a rising bubble is affected by the wall distance and surfactant concentration. The Strouhal number ($St=fd_{eq}/\overline{U}$) is used to evaluate the oscillatory behavior of rising bubbles, where f is the frequency of trajectory. Fig. 6(b) shows the relationship between the Strouhal number and the dimensionless wall distance. The Strouhal number of the clean bubble is linear ($St \sim (0.0967-0.00251S^*)$), where S^* ranges from 0.22 to 7.62, the goodness of fit, R^2, is great than 0.93. The Strouhal number of the contaminated bubble gradually fluctuates within a range as the distance increases ($St \sim (15.5-15.4S^{*2})$), where S^* ranges from 0.22 to 8.52, the goodness of fit, R^2, is great than 0.71. We find that the overall Strouhal number of the clean bubble is smaller than that of the contaminated bubble. The surfactant has more influence on the mean velocity than on the frequency of path. The increased rigidity of the bubble contaminated by surfactant results in a lower mean velocity and a stable frequency of path.

Instantaneous bubble velocity (U) is decomposed into three direction components: wall-normal velocity (u), vertical velocity (v), and spanwise velocity (w). According to the change characteristics of bubble trajectory parameters, we analyzed the instantaneous velocity of bubble collision and free rising under different concentrations, as shown in Fig. 7(a)-(h). In all cases, the wall-normal velocity changes significantly. In Fig. 7(a), (c), (e), and (g), the bubble is attracted by the wall, causing periodic collision with the wall. The wall-normal velocity accelerates and reaches a negative peak before collision. After collision, the wall-normal velocity decreases until its sign changes. As the bubble moves away from the wall, the wall-normal velocity increases to a positive peak. As the bubble bounces back, the same process is repeated.

The viscous dissipation caused by collision changes the instantaneous velocity of the bubble before and after the collision. The peak value of the instantaneous velocity of the clean bubble decreases by approximately 37%. However, as the surfactant concentration increases to 100 ppm, 400 ppm, and 800 ppm, the peak values of the instantaneous velocity decrease by 20%, 14%, and 9%, respectively, which is due to the strong inhibitory effect of surfactants on velocity [12,17]. As the Marangoni stress and the surfactant concentration increase, the deformation of the bubble is reduced, and the conversion between kinetic energy and surface energy is suppressed. Eventually, the impact of the collision is weakened. Sections 3 and 5 provide detailed descriptions of the deformation and energy changes in the bubble with collision.

Compared with that of free-rising bubbles, collision also causes wall-normal velocity of clean bubbles to change periodically along the collision trajectory. The change range of wall-normal velocity decreases by approximately 12%. After surfactant addition, the Marangoni effect occurs, which inhibits bubble movement and reduces the velocity of the bubble. Unlike the clean bubble, collision increases the variation range of the wall-normal velocity of the contaminated bubble. At 100 ppm, the range is increased by 11%. At 400 ppm and 800 ppm, due to the occurrence of collisions, the range increases by 24% and 34%, respectively.

We calculate the frequency of the wall-normal velocity by using the normalized power spectrum [35]. The normalized power spectrum is defined as

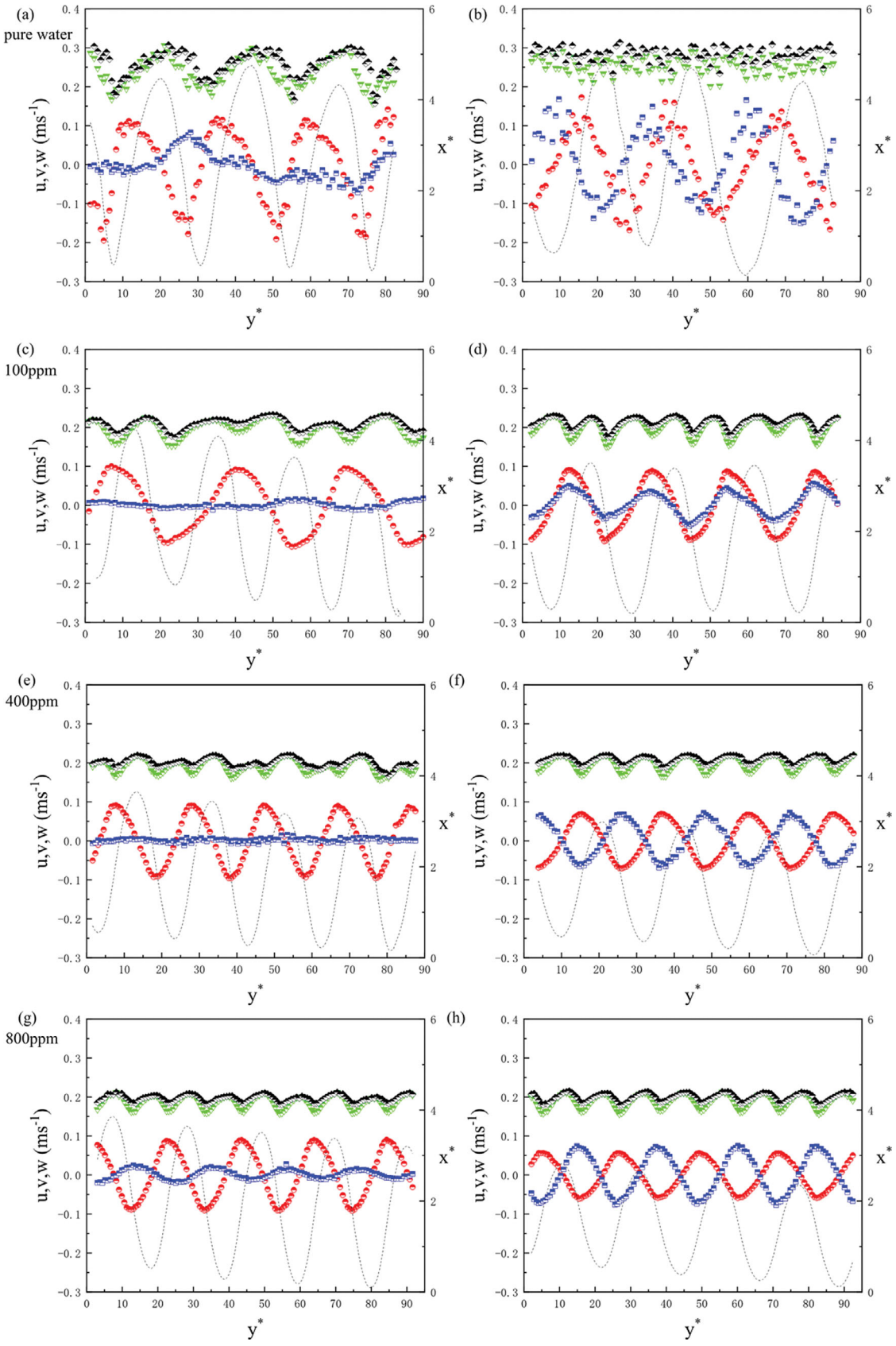

Fig. 7. Effect of various surfactant concentrations on the instantaneous velocity of collision at $S^*\approx0.22$ and the instantaneous velocity of free-rising bubble ($x^*=x/req$, $y^*=y/req$): (a) (c) (e) (g): collision, (b) (d) (f) (h): free-rising case; black: instantaneous velocity (U), green: vertical velocity (v), red: wall-normal velocity (u), blue: spanwise velocity (w), dotted line: the trajectory of bubbles.

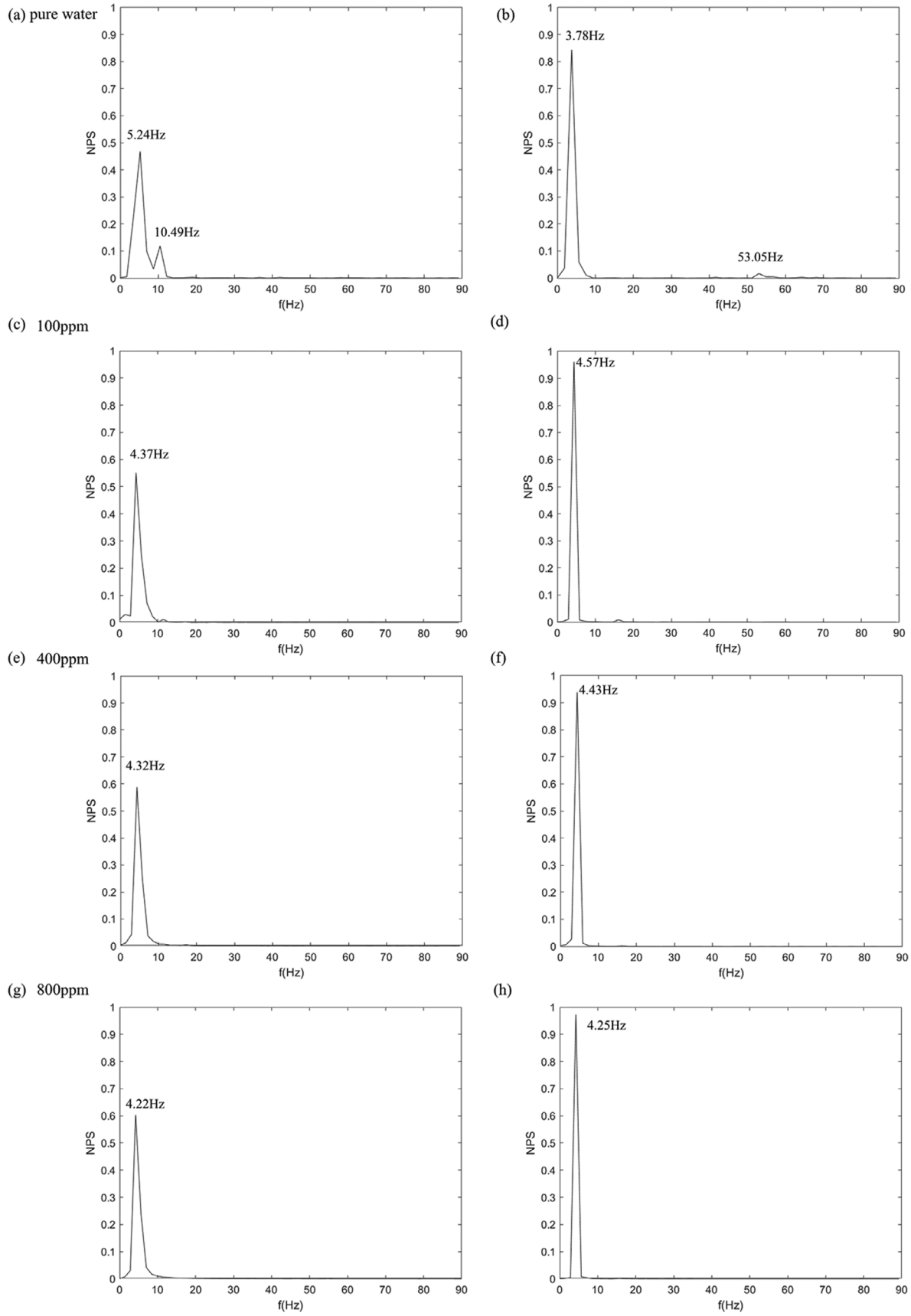

Fig. 8. Effect of various surfactant concentrations on the frequency of wall-normal velocity at $S^* \approx 0.22$ and free-rising case: (a) (c) (e) (g): collision at $S^* \approx 0.22$, (b) (d) (f) (h): free-rising case.

$$NPS[f(t)] = \frac{FFT[f(t)]\overline{FFT[f(t)]}}{\langle FFT[f(t)]\overline{FFT[f(t)]}\rangle} \quad (6)$$

where FFT is the fast Fourier transform, the overline represents the complex conjugate, and < > shows the average value.

Fig. 8 shows the normalized power spectrum of the wall-normal velocity for collision and free rising. Fig. 8(a) and (b) show that under the condition of pure water, the power spectrum amplitude of the wall-normal velocity decreases and the frequency increases due to the existence of a wall. The main peak frequency increases from 3.78 Hz to 5.24 Hz. Under the condition of pure water, the power spectrum shows a secondary peak. The secondary peak frequency changes from 53.05 Hz to 10.49 Hz. In Fig. 7, the wall-normal velocity of clean bubbles fluctuates greatly. As y^* increases,

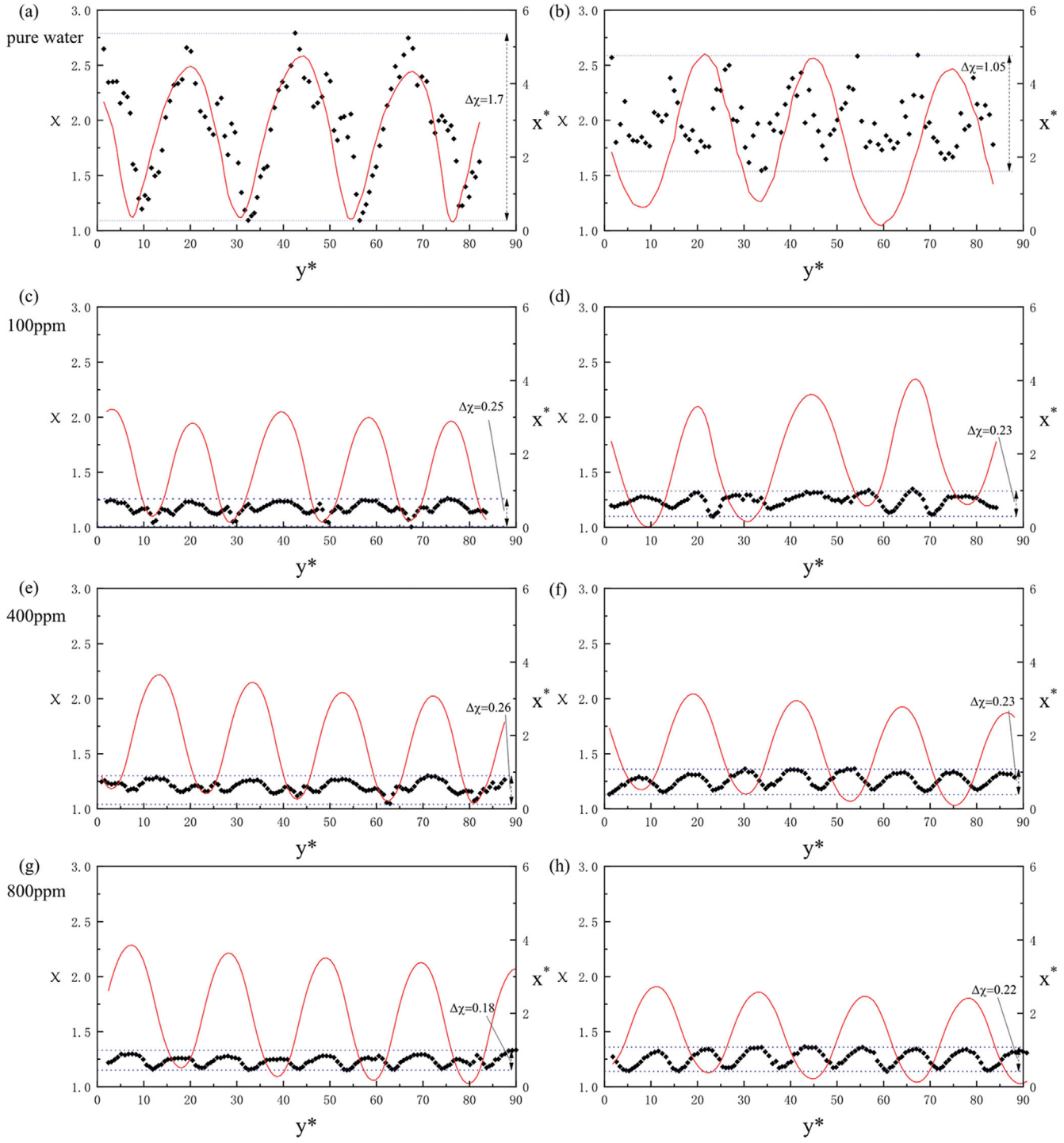

Fig. 9. Effect of various surfactant concentrations on the aspect ratio of collision at $S^* \approx 0.22$ and the free-rising case in the x-y plane: (a) (c) (e) (g): collision at $S^* \approx 0.22$, (b) (d) (f) (h): free-rising case; black point: the aspect ratio of the bubble, red line: the trajectory of the bubble.

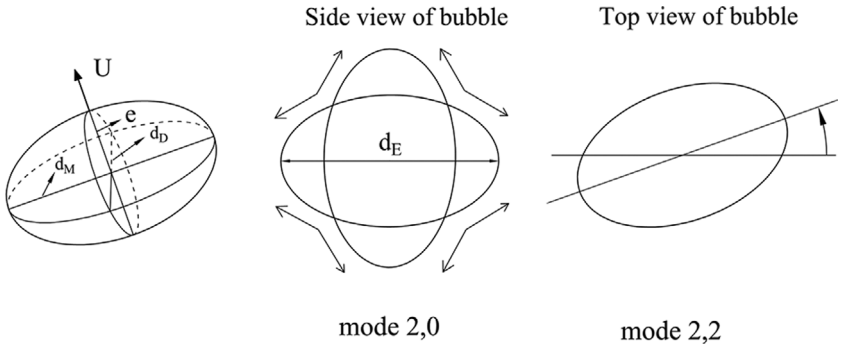

Fig. 10. A sketch of two shape oscillation modes of an ellipsoidal bubble.

a clean bubble appears at the same velocity at adjacent positions. When surfactants are added, the fluctuation of the wall-normal velocity of the contamination bubble is small. At the same y^*, the contamination bubble has a more stable period. The wall-normal velocity of clean bubbles oscillates, which affects the periodic stability. The oscillation of the wall-normal velocity of the clean bubble shows different peaks through FFT, which represents the effect of different factors. The wall-normal velocity oscillation of clean bubbles may be related to bubble deformation. In Fig. 8(c)-(h), as the surfactant concentration increases, the amplitude of the wall-normal velocity power spectrum of collision is augmented. In the case of wall collision, the main peak frequency of the contaminated bubble gradually decreases from 4.37 Hz to 4.22 Hz. However, unlike that of the clean bubble, the main peak frequency of contaminated bubble collision is less than that in the free-rising case. The change in contaminated bubble energy and force caused by collision has an important influence on the change in the frequency of the wall-normal velocity.

3. Oscillation of Shape and Motion

The shape and motion of the contaminated bubble are restrained due to the decrease in surface tension and the Marangoni effect [17,36]. Fig. 9(a)-(h) show the change in the aspect ratio of the bubble ($\chi=d_h/d_v$) with wall collision and free rising at different concentrations. The aspect ratio of the bubble changes along the trajectory. When the bubble moves towards the wall, the aspect ratio gradually decreases until reaching the minimum value, and energy conversion occurs during collision. After collision, the aspect ratio of the bubble gradually rises until reaching the maximum value at the farthest distance from the wall.

As shown in Fig. 9(a) (b), compared with the free-rising clean bubble, the existence of the wall increases the shear and the deformation. The collision increases the mean fluctuation range of the aspect ratio by approximately 38%. However, surfactant addition reduces the aspect ratio of the bubble and inhibits bubble deformation. Under the influence of the Marangoni effect, the conversion between kinetic energy and surface energy is affected. As shown in Fig. 8(c)-(h), the variation range of the aspect ratio of the contaminated bubble collision is different from that of the clean bubble. Compared with that of the free-rising bubble, the fluctuation range of the aspect ratio of bubble collision increases by approximately 8% at 100 ppm and 11% at 400 ppm. There is a little difference in bubble deformation between 100 ppm and 400 ppm due to the impact of the collision. However, when the concentration is 800 ppm, the fluctuation range of the aspect ratio of bubble collision is reduced by 18%.

Bubble deformation causes shape oscillation and affects the motion oscillation [35]. The main axis measured in two images (x-y, y-z) is an accurate projection of the bubble axis. Shape oscillation analysis is entirely based on these results. In Fig. 10, the main axis is represented by a solid line, labelled d_D and d_M. The major and minor axes clearly show that the bubble experiences regular oscillations in shape. Simple conversion is carried out on the axis data to study the obvious property of two-axis oscillations. According to the evolution of the two equivalent main axes of the bubble, shape oscillation can be divided into mode (2, 0) and mode (2, 2). Based on the two spatially equivalent main axes (d_D and d_M) of bubbles, the criteria of the two vibration modes are calculated. For mode (2, 0), the significant in-phase oscillation is explained. The in-phase oscillation of the major axis reflects the fluctuation in the ellipticity of the bubble. The equivalent main axis $d_E=\sqrt{d_D d_M}$ is calculated by observing the change in the equivalent area from the side view to identify mode (2, 0). For mode (2, 2), the main axis corresponds to backward oscillation. The bubble is an ellipsoid rotating around its minor axis e, and its passage through the ratio of the two main axes $R=d_D/d_M$ reveals the mode.

The expressions for the frequencies of the mode (2, 0) and mode (2, 2) are shown in Eqs (7)-(8) [26,35,37]:

$$f_{2,0}=\frac{1}{2\pi}\left(\frac{16\sqrt{2}\tau^2\sigma}{\rho(\tau^2+1)^{3/2}r_{eq}^3}\right)^{1/2} \tag{7}$$

$$f_{2,2}=\frac{1}{2\pi}\left(\frac{8\sigma}{\rho\pi r_{eq}^3}\right)^{1/2} \tag{8}$$

where τ is the ellipticity of the bubble, defined as the ratio of its major to minor axes. A span in ellipticity covers a wide range of bubble sizes: 0.7 mm<r_{eq}<7 mm [34].

As shown in Fig. 11, the frequency of symmetrical shape oscillation is calculated. The frequency of mode (2, 0) is greater than that of mode (2, 2) under the condition of pure water according to the research rules of Veldhuis and Lunde [35,37]. The frequencies of mode (2, 0) and mode (2, 2) show no obvious regular changes with different wall distances. When a bubble is contaminated, the frequency of mode (2, 0) decreases, and the frequency of mode (2, 2) increases. At 100 ppm, the mean frequency of mode (2, 0) de-

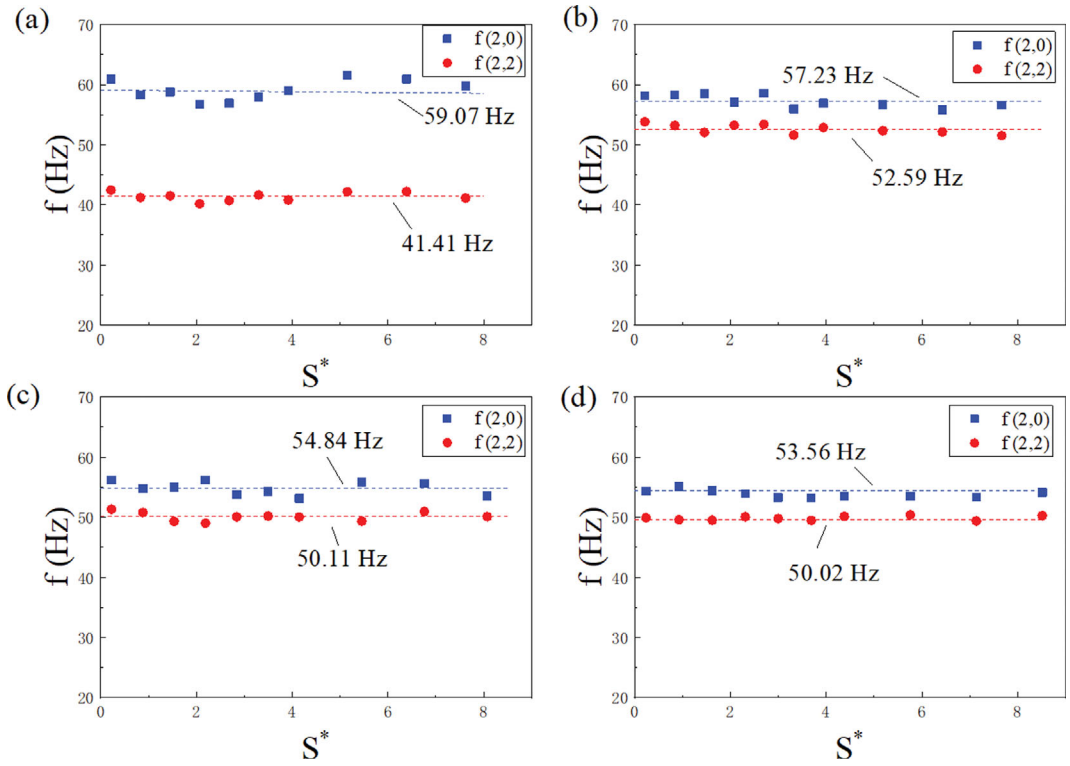

Fig. 11. Effects of the frequency of symmetrical shape oscillation as a function of dimensionless initial wall distance S^* at various surfactant concentrations: (a) pure water, (b) 100 ppm, (c) 400 ppm, and (d) 800 ppm; dashed line: mean frequency.

creases from 59.07 Hz to 57.23 Hz, and the mean frequency of mode (2, 2) increases from 41.41 Hz to 52.59 Hz. At 400 ppm, the mean frequencies of mode (2, 0) and mode (2, 2) are 54.84 Hz and 50.11 Hz, respectively. Compared to those at the 400 ppm concentration, no significant change is observed when the concentration is 800 ppm. The mean frequencies of mode (2, 0) and mode (2, 2) are 53.56 Hz and 50.02 Hz, respectively. As the concentration increases, the oscillation frequency tends to stabilize. The concentration gradient on the surface of the bubble causes the movement of surfactant molecules to form Marangoni shear stress [6,7]. The shear effect on the bubble surface enhances bubble rotation, and the bubble shape gradually approaches a sphere. Therefore, the Marangoni effect promotes the rotating oscillation frequency of mode (2, 2) and suppresses the ellipticity oscillation frequency of mode (2, 0).

4. Force Analysis

The forces acting on a bubble include buoyancy, drag, history, lift, and added mass forces [38]. Kirchhoff's equation is applied to the motion of a bubble to estimate the drag and lift coefficients of the bubble assuming that the bubble inertia can be ignored [39-41]. The Kirchhoff equation can be written as

$$\mathbf{A}_{ij}\frac{\mathrm{d}U_j}{\mathrm{d}_t}+\varepsilon_{ijk}\Omega_j\mathbf{A}_{kl}U_l=F_i+F_{Bi} \tag{9}$$

$$\mathbf{D}_{ij}\frac{\mathrm{d}\Omega_j}{\mathrm{dt}}+\varepsilon_{ijk}\Omega_j\mathbf{D}_{kl}\Omega_l+\varepsilon_{ijk}U_j\mathbf{A}_{kl}U_l=\Gamma_i \tag{10}$$

where **A** and **D** are the added mass and the rotational inertia tensors, respectively. U and Ω are the velocity and rotation velocity, respectively. F and Γ are the hydrodynamic force and torque experienced by the bubble, and ε is a Levi-Civita symbol. Fig. 12 shows an orthogonal coordinate system (1, 2, 3), where 1 corresponds to the bubble velocity vector direction. For a rising bubble in stagnant liquid, F=(F_D+F_{B1}, F_{L2}+F_{B2}, F_{L3}), where F_D, F_L, and F_B are drag, lift, and buoyancy, respectively. History force is implicit in the time dynamics of drag and lift but can be ignored [41]. The

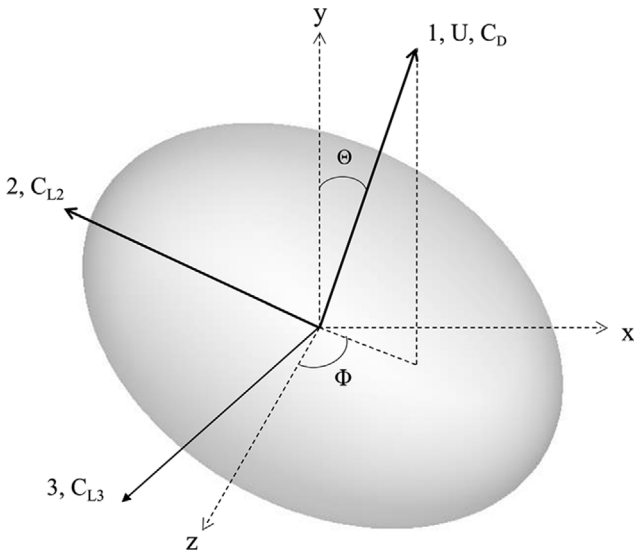

Fig. 12. Schematic of the coordinate system for a bubble.

drag force F_D is the force parallel to the bubble trajectory, and the lift force F_L is the force perpendicular to the bubble trajectory. The symmetry axis of the flat bubble is aligned with the bubble velocity vector. The Kirchhoff equation governs six degrees of freedom to completely specify the angular velocity Ω and the linear velocity U. The 1-direction is always parallel to the velocity vector of the bubble. The 2-direction and 1-direction form a right angle, the 1-2 plane is vertical, and the 3-direction is orthogonal to the 1-direction and 2-direction. Eq. (9), (10) can be simplified as

$$\mathbf{A_{11}}\frac{dU}{dt}=F_D+F_{B1};\ \Omega_3\mathbf{A_{11}}U=F_{L2}+F_{B2};\ -\Omega_2\mathbf{A_{11}}U=F_{L3}$$

$$\Omega_1=\frac{d\phi}{dt}\cos\theta;\ \Omega_2=\frac{d\phi}{dt}\sin\theta;\ \Omega_3=-\frac{d\theta}{dt}$$

$$F_{B1}=\rho V g\cos\theta;\ F_{B2}=\rho V g\sin\theta;\ |F_L|=\sqrt{F_{L2}^2+F_{L3}^2} \quad (11)$$

where θ and ϕ are the polar angle and azimuth angle of the bubble rising path θ=arctan(u/v) and $d\phi/dt=(u\frac{dv}{dt}-v\frac{du}{dt})/u_{xy}^2$, respectively. $\mathbf{A_{11}}$ is expressed as added mass $\mathbf{A}_{11}=C_M\rho V$, C_M is the added mass coefficient, and V is the volume of the bubble [25].

$$C_M=\frac{\alpha}{2-\alpha};\ \alpha=\frac{2\chi^2}{\chi^2-1}\left[1-\frac{1}{\sqrt{\chi^2-1}}\cos^{-1}\left(\frac{1}{\chi}\right)\right] \quad (12)$$

Based on the calculation results, the drag coefficient C_D and lift coefficient C_L of rising bubble are

$$C_D=F_D/(\pi r_{eq}^2\rho U^2/2);\ C_L=F_L/(\pi r_{eq}^2\rho U^2/2) \quad (13)$$

Fig. 13(a) shows the change in the drag coefficient. Under pure water conditions, the velocity fluctuation increases due to the existence of wall shear, which leads to an increase in the drag coefficient. The velocity fluctuation weakens and drag decreases gradually with dimensionless distance [42]. Until the furthest distance is approximately 8.5, the drag coefficient is close to the drag coefficient in the free-rising case. Referring to the velocity field, the drag coefficient of the bubble is found to increase obviously due to collision. After surfactant addition, the surface tension decreases. The bubble surface changes from zero shear to the nonzero shear condition under the influence of the Marangoni effect. As the surfactant concentration increases, the vortex structure becomes stronger, leading to an increase in bubble drag [13,14]. We find that the fluctuation of the drag coefficient decreases near the wall with the surfactant concentration, which corresponds to the velocity field. At 100 ppm and 400 ppm, the drag coefficient of bubble collision is higher than that in the no-collision situation. As the wall distance increases, the drag coefficient fluctuation decreases. However, when the concentration reaches 800 ppm, compared with that in the free-rising case, the drag coefficient does not change significantly with distance, showing that the drag force is mainly affected by the concentration. As the concentration increases, the bubble becomes a solid sphere, and the surface is fixed. The drag coefficient of the bubble is equivalent to that of a rigid sphere of the same size. At this moment, the impact of the collision between the bubble and the wall is small. The Marangoni effect rather than the wall effect predominates.

As shown in Fig. 13(b), to fit the change in C_D between the free-rising bubble and near-wall bubble, the normalized drag coefficient C_D^* is defined as, where C_{D0} is the free-rising drag coefficient. The relationship between C_D^* and S^* obtained from the acrylic case at $2.06<S^*<7.62$ is in good agreement with that in previous experiments with bubbles moving along a rectilinear trajectory ($C_D^*\sim(1+S^{*-3})$), where S^* ranges from 1.11 to 7.62, and the goodness of fit, R^2, is greater than 0.90 [43]. While the relation for the contaminated bubble at $0.22<S^*<8.52$ corresponds to the analytical result ($C_D^*\sim(40.06-39.04S^{*1.203})$), where the goodness of fit, R^2, is great than 0.73. Compared with that of the clean bubble, which transitions from zigzag to spiral movement, the normalized drag coefficient of the contaminated bubble is smaller. As the concentration increases, the rigidity of the bubble increases, causing the wall effect to decrease and the drag coefficient to stabilize.

Fig. 14 shows the lift coefficient as a function of wall distance. The existence of the wall has a considerable influence on the lift coefficient of the clean bubble [44]. The path changes from a zigzag to a three-dimensional spiral, and the lift coefficient of the

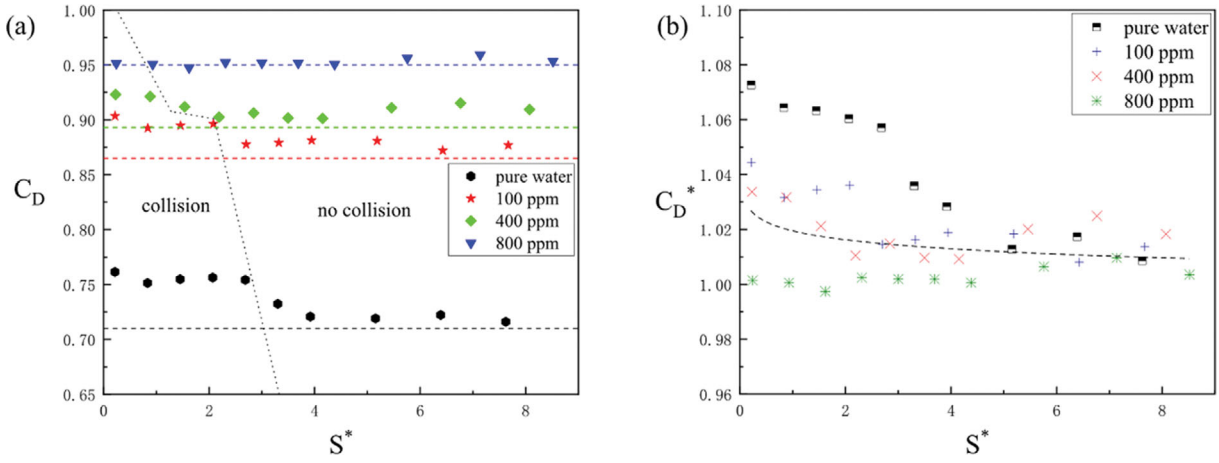

Fig. 13. Effect of drag coefficient C_D and dimensionless drag coefficient C_D^* as a function of dimensionless initial wall distance S^* at various surfactant concentrations: (a) drag coefficient of bubble C_D; dotted line: the free-rising case; (b) dimensionless drag coefficient of bubble C_D^*; dotted line: fitting result of contaminated bubbles.

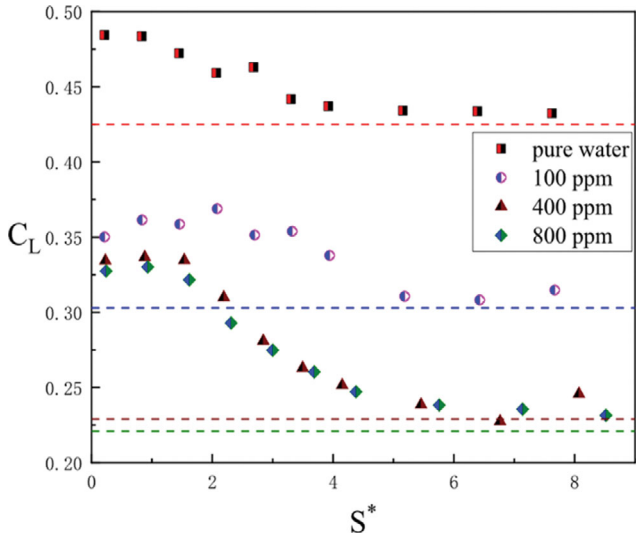

Fig. 14. Effect of lift coefficient C_L as a function of dimensionless initial wall distance S^* at various surfactant concentrations; dotted line: free-rising case.

bubble gradually decreases with the initial wall distance due to the wall-induced lift force pushing the bubble away from the wall. The lift coefficient of the bubble is close to the lift coefficient in the free-rising case, where the dimensionless distance is approximately 8.5. After surfactant addition, the lift coefficient decreased obviously [21,45]. The nonlinear decrease in the lift coefficient is related to the surfactant concentration. As the distance increases, the lift coefficient of the contaminated bubble decreases. At 100 ppm, the lift coefficient decreases compared to that in the clean bubble condition. Interestingly, as the distance increases, the lift coefficients are similar at 400 ppm and 800 ppm. As the concentration increases, the behavior of contaminated bubbles develops towards rigid spheres [12]. The influence of concentration on lift decreases and tends to be stable. The effect of the surfactant concentration on the lift coefficient of the bubble can be neglected.

5. Energy Analysis

As mentioned, when a bubble is close to a wall, especially in the process of collision with the wall, energy conversion cannot be ignored. We analyzed energy conversion with collision between the wall and bubble under different surfactant concentrations, includ-

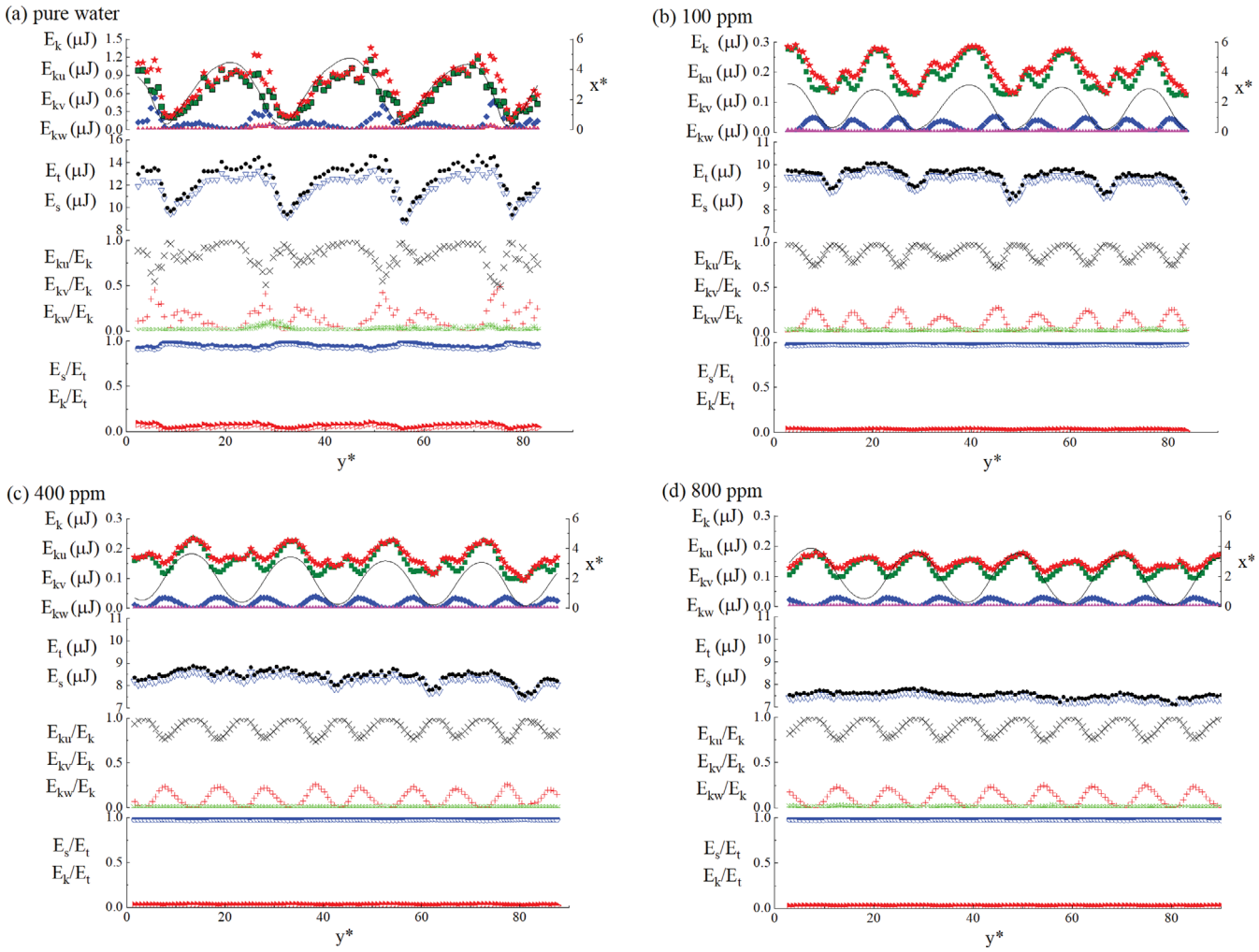

Fig. 15. Effect of various surfactant concentrations on energy variations of bubble collision at S^*≈0.22; (★) E_k; (◆) E_{ku}; (■) E_{kv}; (▲) E_{kw}; (●) E_t; (▽) E_s; (×) E_{kv}/E_k; (+) E_{ku}/E_k; (★) E_{kv}/E_k; (●) E_s/E_t; (▶) E_s/E_t.

ing surface energy E_s and kinetic energy E_k. The kinetic energy E_k and surface energy E_s of the bubble can be calculated [25]:

$$E_k = \frac{1}{2}(\rho_g + C_M\rho_l)V(u^2+v^2+w^2) = E_{ku} + E_{kv} + E_{kw} \quad (14)$$

$$E_S = \sigma A \quad (15)$$

$$A = \frac{\pi d_h^2}{2}\left(1+\frac{1-e^2}{e}\tanh^{-1}e\right),\ e^2 = 1-\chi^{-2} \quad (16)$$

$$E_t = E_k + E_s \quad (17)$$

where E_{ku}, E_{kv}, and E_{kw} are the three components of the total kinetic energy E_k. E_t is the sum of kinetic energy and surface energy.

In Fig. 15, the energy change with bubble-wall collision is shown at $S^*\approx0.22$, and changes in the surface energy and kinetic energy are observed. When the bubble is close to the wall, the kinetic energy E_k rapidly decreases during the collision. After surfactant addition, we find that the kinetic energy E_k, E_{ku}, E_{kv}, and E_{kw} decrease due to the Marangoni effect. E_{ku} is more periodically affected by bubble deformation and velocity. E_{kw} is consistent with the change in velocity in the spanwise direction, and the growth along y^* is almost unchanged. The surface energy of the bubble decreases with the surfactant concentration. The maximum surface energy of a clean bubble is 13.2 μJ. When the concentration is 100 ppm, the maximum surface energy is 9.8 μJ. The maximum value is 8.6 μJ at 400 ppm. At 800 ppm, the surface energy continues to decrease, and the maximum value is 7.6 μJ. Due to the inhibitory effect of surfactant on bubble deformation and the decrease in the surface tension of the liquid, the change in the surface energy of the contaminated bubble gradually decreases during collision.

The total energy E_t is affected by the surface energy and total kinetic energy and changes periodically along the trajectory of bubble collision. At the time of collision, the total energy reaches its minimum value. We find that as the concentration increases, the total energy change in the bubble gradually decreases. Affected by the Marangoni effect, the total energy of the clean bubble during collision is greater than that of the contaminated bubble. The total energy range under pure water conditions is 14.62-8.92. At 100 ppm, 400 ppm, and 800 ppm, the total energy range is 10.07-8.46, 8.87-7.54, and 7.82-7.11, respectively, and the range of change is 5.7, 1.61, 1.33, and 0.71, respectively. As the surfactant concentration increases, the surface activity of the bubbles and the internal circulation flow are inhibited, resulting in the bubble behaving similar to a rigid sphere.

Surfactant affects the ratio of the kinetic energy components to total kinetic energy in three directions. Compared with those in pure water, the proportion of E_{kv} is increased, and the proportion of E_{ku} is decreased. As the surfactant concentration increases from 100 ppm to 400 and 800 ppm, the minimum values of the kinetic energy ratio in the vertical direction (E_{kv}/E_k) increase by 0.72, 0.73, and 0.74, and the maximum ratios of kinetic energy in the wall-normal direction (E_{ku}/E_k) decrease by 0.27, 0.26, and 0.25, respectively. Surfactants also affect the ratio of kinetic energy and surface energy to the total energy. The proportion of surface energy is far greater than that of kinetic energy. Surfactants reduce the fluctuation of the ratio of kinetic energy and surface energy to total energy. As y^* increases, the ratio of kinetic energy and surface energy to total energy remains almost unchanged. Thus, the surfactant has a considerable influence on the conversion of surface energy and kinetic energy and inhibits the deformation and motion caused by bubble-wall collision. As the surfactant concentration increases, the Marangoni effect enhances the inhibition of the wall-normal kinetic energy of the bubble and weakens the influence of the wall effect on the bubble.

CONCLUSION

The current work presents detailed information on the dynamic behavior of an ellipsoidal contaminated bubble (Re≈470-800) with different initial dimensionless wall distances and surfactant (SDS) concentrations (100 ppm, 400 ppm, 800 ppm), which helps improve the understanding of dynamic behavior mechanism and provides a reference for chemical, nuclear and environmental industries. Due to the gradient of surface tension, the dynamic behavior of bubbles is affected by the Marangoni stress on bubbles.

(i) SDS inhibits the transverse movement of bubbles and accelerates the transformation from zigzag trajectory to spiral trajectory. The critical initial dimensionless distance at which the collision occurs S^* is decreased due to a dimensionless distance change from 3.3 to 0.23.

(ii) SDS reduces the velocity of bubbles and increases the drag of bubbles near the vertical wall. The wall-normal velocity of the contaminated bubble has a more stable period.

(iii) SDS inhibits the deformation range of bubbles. Meanwhile, the frequency of mode (2, 2) bubble rotation is increased and the frequency of mode (2, 0) elliptic oscillation is decreased.

(iv) As the SDS concentration increases, the wall effect is suppressed. After 800 ppm ($Mo=2.65\times10^{-10}$, σ=42.24 mN/m), the Marangoni effect dominates. The effect of wall boundary can be ignored. Due to both wall shear stress and Marangoni shear stress affecting bubbles simultaneously, the dominant factors of bubble behavior near the wall are different at various concentrations. At 800 ppm, the mean velocity and drag remain almost unchanged with distance variation. The wavelength of trajectory and lift coefficient does not change with increasing concentration. The deformation range of bubble near the wall is lower than that of the bubble rising freely. The conversion between kinetic energy and surface energy is changed, which weakens the impact of the bubble-wall collision.

ACKNOWLEDGEMENTS

This research is supported by the National Natural Science Foundation of China (11572357, 11602077) and Natural Science Foundation of Hebei Province, China (A2021202009).

NOMENCLATURE

Non-dimensional Numbers

Eo : Eötvös number, $Eo=gd_{eq}^2(\rho_l-\rho_g)\sigma^{-1}$ [-]
Mo : Morton number, $Mo=(\rho_l-\rho_g)g\mu_l^4\sigma^{-3}\rho_l^{-2}$ [-]
Re : Reynolds number, $Re=\rho_l U d_{eq}\mu^{-1}$ [-]
St : Strouhal number, $St=fd_{eq}/\overline{U}$ [-]

We : Weber number, We=$\rho_l U^2 d_{eq} \sigma^{-1}$ [-]

Symbols

A : surface area [mm^2]
$\mathbf{A}_{ij}$: added mass tensor [-]
C : surfactant concentration [ppm]
C_D : drag coefficient [-]
C_L : lift coefficient [-]
C_M : added mass coefficient [-]
d_{eq} : equivalent diameter [mm]
d_h : horizontal axis of in a plane of the bubble [mm]
d_v : vertical axis of in a plane of the bubble [mm]
d_D : major axis of the bubble (y-z) [mm]
d_M : major axis of the bubble (x-y) [mm]
$\mathbf{D}_{ij}$: rotational inertia tensor [-]
e : minor axis of the bubble [mm]
E_k : kinetic energy [μJ]
E_s : surface energy [μJ]
E_t : total energy [μJ]
f : frequency of trajectory [Hz]
f(2, 0) : frequency of shape oscillation (2, 0) [Hz]
f(2, 2) : frequency of shape oscillation (2, 2) [Hz]
g : gravity acceleration [ms^{-2}]
h : amplitude [mm]
F_B : buoyancy [N]
F_D : drag force [N]
F_L : lift force [N]
l : elevation [mm]
r : horizontal shift of the periodic trajectory [mm]
r_{eq} : equivalent radius [mm]
S : initial wall distance [-]
S^* : initial dimensionless wall distance, $S^*=S/r_{eq}$ [-]
t : time interval between two frames of a photograph [s]
u : wall-normal velocity [ms^{-1}]
U : instantaneous velocity of bubble [ms^{-1}]
$\overline{U}$: mean velocity of bubble [ms^{-1}]
v : vertical velocity [ms^{-1}]
V : volume of bubble [mm^3]
w : spanwise velocity [ms^{-1}]
x, y, z : Cartesian co-ordinates [mm]

Greek Symbols

ρ : density [kgm^{-3}]
σ : surface tension [Nm^{-1}]
μ : dynamic viscosity [Nsm^{-2}]
λ : wavelength [mm]
τ : ellipticity of the bubble [-]
χ : aspect ratio [-]
θ : the polar angle of the bubble rising path [rad]
ϕ : azimuth angle of the bubble rising path [rad]
Ω : rotation velocity [rad/s]
Γ : torque [Nm]
ε : Levi-Civita symbol [-]

Subscripts

g : gas phase
i : corresponding components on the coordinate axis
l : liquid phase
u, v, w : corresponding components to the direction of velocity
x, y, z : corresponding components in x, y, z-direction
0 : free-rising bubble

Superscripts

* : dimensionless quantity

REFERENCES

1. M. K. Tripathi, K. C. Sahu and R. Govindarajan, *Nat. Commun.*, **6**, 1 (2015).
2. S. Takagi and Y. Matsumoto, *Annu. Rev. Fluid Mech.*, **43**, 1 (2011).
3. Z. Ahmed, D. Izbassarov, J. Lu, G. Tryggvason, M. Muradoglu and O. Tammisola, *Int. J. Multiph. Flow*, **126**, 1 (2020).
4. M. Muradoglu and G. Tryggvason, *J. Comput. Phys.*, **274**, 1 (2014).
5. H. A. Stone, *Annu. Rev. Fluid Mech.*, **26**, 1 (1994).
6. S. Hosokawa, K. Hayashi and A. Tomiyama, *Int. J. Multiph. Flow*, **97**, 1 (2017).
7. S. Hosokawa, K. Hayashi and A. Tomiyama, *Exp. Therm. Fluid Sci.*, **96**, 1 (2018).
8. S. Takagi and Y. Matsumoto, *Annu. Rev. Fluid Mech.*, **43**, 1 (2011).
9. M. Fukuta, S. Takagi and Y. Matsumoto, *Phys. Fluids*, **20**, 4 (2008).
10. Y. Tagawa, S. Takagi and Y. Matsumoto, *J. Fluid Mech.*, **738**, 1 (2014).
11. D. Rodrigue, D. De Kee and C. C. M. Fong, *J. Non-Newton Fluid Mech.*, **66**, 1 (1996).
12. S. Tasoglu, U. Demirci and M. Muradoglu, *Phys. Fluids*, **20**, 4 (2008).
13. B. Cuenot, J. Magnaudet and B. Spennato, *J. Fluid Mech.*, **339**, 25 (1997).
14. Y. Fei and M. Pang, *Int. J. Heat Mass Transfer*, **121**, 1 (2018).
15. F. Raymond and J. M. Rosant, *Chem. Eng. Sci.*, **55**, 5 (2000).
16. A. Tzounakos, D. G. Karamanev, A. Margaritis and M. A. Bergougnou, *Ind. Eng. Chem. Res.*, **43**, 18 (2004).
17. S. Aoyama, K. Hayashi, S. Hosokawa and A. Tomiyama, *Exp. Therm. Fluid Sci.*, **96**, 1 (2018).
18. R. Clift, J. R. Grace and M. E. Weber, *Bubbles, drops, and particles*, Academic Press, New York (1978).
19. A. W. G. De Vries, A. Biesheuvel and L. Van Wijngaarden, *Int. J. Multiph. Flow*, **28**, 11 (2002).
20. F. Takemura, S. Takagi, J. Magnaudet and Y. Matsumoto, *J. Fluid Mech.*, **461**, 1 (2002).
21. F. Takemura and J. Magnaudet, *J. Fluid Mech.*, **495**, 1 (2003).
22. K. Sugiyama and F. Takemura, *J. Fluid Mech.*, **662**, 1 (2010).
23. K. Sugioka and T. Tsukada, *Int. J. Multiph. Flow*, **71**, 32 (2015).
24. A. Zaruba, D. Lucas, H. M. Prasser and T. Höhne, *Chem. Eng. Sci.*, **62**, 6 (2007).
25. H. Jeong and H. Park, *J. Fluid Mech.*, **771**, 564 (2015).
26. Y. Chen, C. Tu, Q. Yang, Y. Wang and F. Bao, *Exp. Therm. Fluid Sci.*, **120**, 110235 (2021).
27. J. Zhang and M.-J. Ni, *J. Fluid Mech.*, **828**, 1 (2017).
28. A. Tomiyama, G. P. Celata, S. Hosokawa and S. Yoshida, *Int. J. Multiph. Flow*, **28**, 9 (2002).
29. A. Busciglio, G. Vella, G. Micale and L. Rizzuti, *Chem. Eng. J.*, **140**, 1 (2008).
30. G. P. Celata, F. D'Annibale, P. Di Marco, G. Memoli and A. Tomi-

yama, *Exp. Therm. Fluid Sci.*, **31**, 6 (2007).
31. R. Zenit and J. Magnaudet, *Int. J. Multiph. Flow*, **35**, 2 (2009).
32. J. Lee and H. Park, *Int. J. Multiph. Flow*, **91**, 1 (2017).
33. J. Huang and T. Saito, *Chem. Eng. Sci.*, **170**, 105 (2017).
34. B. Figueroa-Espinoza, R. Zenit and D. Legendre, *J. Fluid Mech.*, **616**, 419 (2008).
35. C. Veldhuis, A. Biesheuvel and L. Van Wijngaarden, *Phys. Fluids*, **20**, 4 (2008).
36. R. Bel Fdhila and P. C. Duineveld, *Phys. Fluids*, **8**, 2 (1996).
37. K. Lunde and R. J. Perkins, *Appl. Sci. Res.*, **58**, 387 (1998).
38. J. Magnaudet and I. Eames, *Annu. Rev. Fluid Mech.*, **32**, 1 (2000).
39. G. Mougin and J. Magnaudet, *Int. J. Multiph. Flow*, **28**, 11 (2002).
40. W. L. Shew, S. Ponect and J. F. Pinton, *J. Fluid Mech.*, **569**, 51 (2006).
41. H. Kusuno, H. Yamamoto and T. Sanada, *Phys. Fluids*, **31**, 7 (2019).
42. M. F. Moctezuma, R. Lima-Ochoterena and R. Zenit, *Phys. Fluids*, **17**, 9 (2005).
43. B. Figueroa-Espinoza, R. Zenit and D. Legendre. *J. Fluid Mech.*, **616**, 1 (2008).
44. J. Feng and I. A. Bolotnov, *Int. J. Multiph. Flow*, **99,** 1 (2018).
45. K. Hayashi and A. Tomiyama, *Int. J. Multiph. Flow*, **99**, 1 (2018).